Half-quantum vortex state in a spin-orbit-coupled Bose-Einstein condensate

B. Ramachandhran,[1] Bogdan Opanchuk,[2] Xia-Ji Liu,[2] Han Pu,[1] Peter D. Drummond,[2] and Hui Hu[2]
[1]*Department of Physics and Astronomy, and Rice Quantum Institute, Rice University, Houston, Texas 77251, USA*
[2]*ARC Centres of Excellence for Quantum-Atom Optics and Centre for Atom Optics and Ultrafast Spectroscopy, Swinburne University of Technology, Melbourne 3122, Australia*
(Received 6 January 2012; published 6 February 2012)

We theoretically investigate the condensate state and collective excitations of a two-component Bose gas in a two-dimensional harmonic trap subject to isotropic Rashba spin-orbit coupling. In the weakly interacting regime when the interspecies interaction is larger than the intraspecies interaction ($g_{\uparrow\downarrow} > g$), we find that the condensate ground state has a half-quantum angular momentum vortex configuration with spatial rotational symmetry and skyrmion-type spin texture. Upon increasing the interatomic interaction beyond a threshold g_c, the ground state starts to involve higher-order angular momentum components and thus breaks rotational symmetry. In the case of $g_{\uparrow\downarrow} < g$, the condensate becomes unstable toward the superposition of two degenerate half-quantum vortex states. Both instabilities (at $g > g_c$ and $g_{\uparrow\downarrow} < g$) can be determined by solving the Bogoliubov equations for collective density oscillations of the half-quantum vortex state and by analyzing the softening of mode frequencies. We obtain the phase diagram as a function of the interatomic interactions and the spin-orbit coupling. In addition, we directly simulate the time-dependent Gross-Pitaevskii equation to examine the dynamical properties of the system. Finally, we investigate the stability of the half-quantum vortex state against both trap anisotropy and anisotropy in the spin-orbit coupling.

DOI: 10.1103/PhysRevA.85.023606 PACS number(s): 03.75.Mn, 05.30.Jp, 67.85.Fg, 67.85.Jk

I. INTRODUCTION

Owing to unprecedented control of interatomic interaction, geometry, and purity, atomic quantum gases have proven to be an ideal platform for exploring fundamental many-body quantum states, such as Bose-Einstein condensates (BECs) [1], strongly interacting unitary Fermi superfluids [2,3], and Mott-insulating states [4]. One of the latest achievements concerns spin-orbit (SO) coupling in an ultracold spinor Bose gas of ^{87}Rb atoms [5], induced by so-called "synthetic non-Abelian gauge fields." Novel quantum states may be anticipated in the presence of SO coupling [6–19]. Indeed, for a homogeneous SO-coupled spin-1/2 Bose gas with intra- and interspecies interactions (g and $g_{\uparrow\downarrow}$), a single plane-wave or a density-stripe condensate state has been predicted [8], depending on whether g is larger or smaller than $g_{\uparrow\downarrow}$. Interesting density patterns have been observed in the theoretical simulations for an SO-coupled spinor condensate, in the absence [8,12,13,18,19] or presence [15–17] of rotation. The phenomenon of self-trapped BECs has been proposed in one-dimensional (1D) geometries [7]. The critical temperature of SO coupled Bose gases in harmonic traps has also been studied [20].

In this work, we show that, in a Rashba SO-coupled, weakly interacting spin-1/2 Bose gas in a two-dimensional (2D) harmonic trap, all bosons may condense into a nontrivial half-integer angular momentum state (or a half-quantum vortex state) with a skyrmion-type spin texture. Our study is motivated by the real experiment, where a harmonic trap is necessary to prevent the atoms from escaping. We solve the mean-field Gross-Pitaevskii equation (GPE) for the density distributions and spin textures and obtain the collective excitation spectrum by solving the Bogoliubov equation and also by directly simulating the real-time propagation of the GPE ground state under perturbations. The condensation of an SO-coupled spin-1/2 Bose gas into a half-quantum vortex configuration was first suggested by Congjun Wu and coworkers in 2008, and its existence was discussed under the condition that the interaction is SU(2) symmetric (i.e., $g = g_{\uparrow\downarrow}$ [14]). Here, we explore systematically the parameter space for the half-quantum vortex state and analyze its stability. We present a phase diagram for the half-quantum vortex state as a function of the SO coupling and the interatomic interaction strengths. We also investigate the dynamical properties of the half-quantum vortex state by directly simulating the corresponding time-dependent GPE. Finally, the stability of the half-quantum vortex state against both trap anisotropy and anisotropy in the spin-orbit-coupling term is examined.

Our main results are summarized in Fig. 1. The half-quantum vortex state (the phase I) is the ground state if the intraspecies interaction is smaller than the interspecies interaction ($g < g_{\uparrow\downarrow}$) and if the interaction strength is below a threshold ($g < g_c$), where g_c depends on the ratio of $g_{\uparrow\downarrow}/g$. Otherwise, it becomes energetically unstable toward a superposition state of two degenerate half-quantum vortex states (phase II A), or a state involving higher-order angular momentum components (phase II B). With decreasing dimensionless SO-coupling strength λ_{SO}, the threshold g_c becomes exponentially large, leading to a large parameter space for the half-quantum vortex state (see Fig. 14). It is therefore feasible to observe this in current experiments with ultracold SO-coupled spinor Bose gases of ^{87}Rb atoms.

The rest of the paper is organized as follows: In the next section, we outline the model Hamiltonian and discuss briefly the existence of a half-quantum vortex state in the noninteracting limit. In Sec. III, we present the numerical procedure of solving the GPE and Bogoliubov equations and discuss the typical density distributions and collective mode behavior of the half-quantum vortex state. The collective excitation spectrum obtained from the Bogoliubov equation is compared to a direct simulation of the time-dependent GPE. In Sec. IV, we analyze the stability of the half-quantum

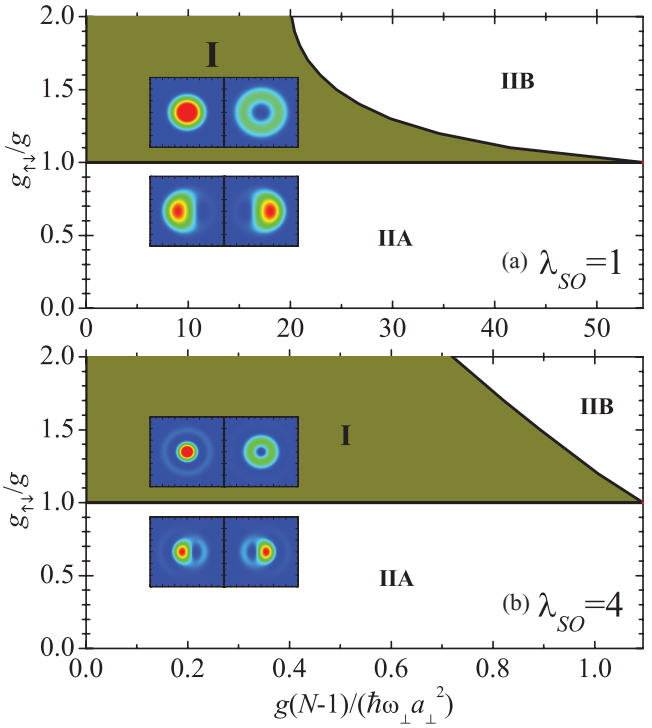

FIG. 1. (Color online) Phase diagram at two dimensionless SO coupling strengths, $\lambda_{\rm SO} = 1$ (a) and $\lambda_{\rm SO} = 4$ (b). The half-quantum vortex state (phase I) becomes unstable when the intraspecies interaction is larger than the interspecies interaction ($g > g_{\uparrow\downarrow}$, phase II A) or when the interatomic interactions are sufficiently strong ($g > g_c$, phase II B). The insets show the density patterns of spin-up and spin-down bosons in phases I and II A. We note that the critical interaction strength g_c increases rapidly with decreasing SO-coupling strength $\lambda_{\rm SO}$.

vortex state by monitoring the softening of collective mode frequencies and by comparing the energy with that of some competing states. The phase diagram is then constructed as a function of interatomic interactions and SO coupling. The stability against anisotropy in the trapping potential and in the spin-orbit coupling term is also carefully examined. Finally, in Sec. V we summarize and give concluding remarks.

II. THEORETICAL FRAMEWORK

We consider a two-component Bose gas confined by a 2D isotropic harmonic trap potential $V(\rho) = M\omega_\perp^2(x^2+y^2)/2 = M\omega_\perp^2\rho^2/2$ with a Rashba SO coupling $\mathcal{V}_{\rm SO} = -i\lambda_{\rm R}(\hat{\sigma}_x\partial_y - \hat{\sigma}_y\partial_x)$, where $\lambda_{\rm R}$ is the Rashba SO coupling strength and $\hat{\sigma}_x$, $\hat{\sigma}_y$, and $\hat{\sigma}_z$ are the 2×2 Pauli matrices. The model Hamiltonian $\mathcal{H} = \int d\mathbf{r}[\mathcal{H}_0 + \mathcal{H}_{\rm int}]$ is given by

$$\mathcal{H}_0 = \Psi^\dagger\left[-\frac{\hbar^2\nabla^2}{2M} + V(\rho) + \mathcal{V}_{\rm SO} - \mu\right]\Psi, \tag{1}$$

$$\mathcal{H}_{\rm int} = (g/2)\sum_{\sigma=\uparrow,\downarrow}\Psi_\sigma^\dagger\Psi_\sigma^\dagger\Psi_\sigma\Psi_\sigma + g_{\uparrow\downarrow}\Psi_\uparrow^\dagger\Psi_\uparrow\Psi_\downarrow^\dagger\Psi_\downarrow, \tag{2}$$

where $\mathbf{r} = (x,y)$ and $\Psi = [\Psi_\uparrow(\mathbf{r}),\Psi_\downarrow(\mathbf{r})]^T$ denotes the spinor Bose field operators. The chemical potential μ is to be determined by the total number of bosons N (i.e., $\int d\mathbf{r}\Psi^\dagger\Psi = N$). For simplicity, we have assumed equal intraspecies interaction strength, so that $g_{\uparrow\uparrow} = g_{\downarrow\downarrow} = g$. In experiments, the two-dimensional geometry can be realized by imposing a strong harmonic potential $V(z) = M\omega_z^2 z^2/2$ along the axial direction in such a way so that $\mu, k_BT \ll \hbar\omega_z$ [21]. For the realistic case of ^{87}Rb atoms, the interaction strengths can be calculated from the two s-wave scattering lengths $a \simeq 100a_B$ and $a_{\uparrow\downarrow}$, using $g = \sqrt{8\pi}(\hbar^2/M)(a/a_z)$ and $g_{\uparrow\downarrow} = \sqrt{8\pi}(\hbar^2/M)(a_{\uparrow\downarrow}/a_z)$, respectively. Here $a_z = \sqrt{\hbar/(M\omega_z)}$ is the characteristic oscillator length in the z direction. Note that here we consider a weakly interacting regime with $a_z \gg a, a_{\uparrow\downarrow}$. In the strongly interacting regime where $a_z \sim a, a_{\uparrow\downarrow}$, one needs to include the confinement-induced resonance in the calculation of 2D interaction parameters g and $g_{\uparrow\downarrow}$ [22]. Note also that, in the recent experiment reported by the Spielman group, a spinor (spin-1) Bose gas of ^{87}Rb atoms with $F = 1$ ground electronic manifold is used. However, to create SO coupling, two internal "spin" states have been selected from the $F = 1$ manifold and have been labeled as pseudo-spin-up and pseudo-spin-down [5]. This gives an effective spin-1/2 Bose gas.

A. Gross-Pitaevskii equation and Bogoliubov equations

For a weakly interacting Bose gas at zero temperature, we assume that all the bosons condense into a single quantum state $\Phi(\mathbf{r}) = [\Phi_\uparrow(\mathbf{r}),\Phi_\downarrow(\mathbf{r})]^T$. Following the standard mean–field theory approach [23], we separate the field operator into a condensate and a fluctuation part, $\Psi_\sigma(\mathbf{r}) = \Phi_\sigma(\mathbf{r}) + \tilde{\Psi}_\sigma(\mathbf{r})$. Keeping up to quadratic terms in $\tilde{\Psi}_\sigma(\mathbf{r})$, this separation leads to an approximate Hamiltonian $\mathcal{H} = \int d\mathbf{r}[\mathcal{H}_{\rm GP} + \mathcal{H}_T]$, where the condensate part is given by

$$\mathcal{H}_{\rm GP} = \Phi^\dagger[\mathcal{H}_{\rm osc} + \mathcal{V}_{\rm SO} - \mu]\Phi + \frac{g}{2}(|\Phi_\uparrow|^4 + |\Phi_\downarrow|^4) + g_{\uparrow\downarrow}|\Phi_\uparrow\Phi_\downarrow|^2, \tag{3}$$

and the fluctuation part is $\mathcal{H}_T = \tilde{\Psi}^\dagger\mathcal{H}_{\rm Bog}\tilde{\Psi}$, where

$$\mathcal{H}_{\rm Bog} = \begin{bmatrix} \mathcal{H}_{s_\uparrow} + g|\Phi_\uparrow|^2 & V_{\rm so} + g_{\uparrow\downarrow}\Phi_\uparrow\Phi_\downarrow^* & g\Phi_\uparrow^2 & g_{\uparrow\downarrow}\Phi_\uparrow\Phi_\downarrow \\ V_{\rm so}^\dagger + g_{\uparrow\downarrow}\Phi_\uparrow^*\Phi_\downarrow & \mathcal{H}_{s_\downarrow} + g|\Phi_\downarrow|^2 & g_{\uparrow\downarrow}\Phi_\uparrow\Phi_\downarrow & g\Phi_\downarrow^2 \\ g(\Phi_\uparrow^*)^2 & g_{\uparrow\downarrow}\Phi_\uparrow^*\Phi_\downarrow^* & \mathcal{H}_{s_\uparrow} + g|\Phi_\uparrow|^2 & -V_{\rm so}^\dagger + g_{\uparrow\downarrow}\Phi_\uparrow^*\Phi_\downarrow \\ g_{\uparrow\downarrow}\Phi_\uparrow^*\Phi_\downarrow^* & g(\Phi_\downarrow^*)^2 & -V_{\rm so} + g_{\uparrow\downarrow}\Phi_\uparrow\Phi_\downarrow^* & \mathcal{H}_{s_\downarrow} + g|\Phi_\downarrow|^2 \end{bmatrix}. \tag{4}$$

Here, $\mathcal{H}_{\rm osc}\equiv -\hbar^2\nabla^2/(2M)+V(\rho)$, $\mathcal{H}_{s_\uparrow}\equiv\mathcal{H}_{\rm osc}+g\|\Phi_\uparrow\|^2+g_{\uparrow\downarrow}\|\Phi_\downarrow\|^2-\mu$, $\mathcal{H}_{s_\downarrow}\equiv\mathcal{H}_{\rm osc}+g_{\uparrow\downarrow}\|\Phi_\uparrow\|^2+g\|\Phi_\downarrow\|^2-\mu$, $V_{\rm so}\equiv -i\lambda_{\rm R}(\partial_y+i\partial_x)$, and $V_{\rm so}^\dagger\equiv -i\lambda_{\rm R}(\partial_y-i\partial_x)$, and we have introduced a 4×4 Nambu spinor $\tilde\Psi=[\tilde\Psi_\uparrow(\mathbf{r}),\tilde\Psi_\downarrow(\mathbf{r}),\tilde\Psi_\uparrow^\dagger(\mathbf{r}),\tilde\Psi_\downarrow^\dagger(\mathbf{r})]^T$.

The condensate wave function can be obtained from the GP equations $\delta\mathcal{H}_{\rm GP}/\delta\Phi(\mathbf{r})=0$ [23] or, explicitly,

$$\begin{bmatrix}\mathcal{H}_{s_\uparrow} & -i\lambda_{\rm R}(\partial_y+i\partial_x)\\ -i\lambda_{\rm R}(\partial_y-i\partial_x) & \mathcal{H}_{s_\downarrow}\end{bmatrix}\begin{bmatrix}\Phi_\uparrow(\mathbf{r})\\ \Phi_\downarrow(\mathbf{r})\end{bmatrix}=0. \quad (5)$$

At zero temperature, we assume a single condensate state with *zero* quantum depletion, so that the condensate wave function is normalized by $\int d\mathbf{r}[\|\Phi_\uparrow\|^2+\|\Phi_\downarrow\|^2]=N$, where N is the total number of bosons. The equation is simplified if we write $\Phi_\uparrow=N^{1/2}\phi_\uparrow$ and $\Phi_\downarrow=N^{1/2}\phi_\downarrow$ and use corresponding interaction strengths $g(N-1)$ and $g_{\uparrow\downarrow}(N-1)$. The normalization condition becomes $\int d\mathbf{r}\,[\|\phi_\uparrow\|^2+\|\phi_\downarrow\|^2]=1$.

The quasiparticle wave functions with energy $\hbar\omega$ satisfy the Bogoliubov equations [23],

$$\mathcal{H}_{\rm Bog}\begin{bmatrix}u_\uparrow(\mathbf{r})\\ u_\downarrow(\mathbf{r})\\ v_\uparrow(\mathbf{r})\\ v_\downarrow(\mathbf{r})\end{bmatrix}=\hbar\omega\begin{bmatrix}+u_\uparrow(\mathbf{r})\\ +u_\downarrow(\mathbf{r})\\ -v_\uparrow(\mathbf{r})\\ -v_\downarrow(\mathbf{r})\end{bmatrix}, \quad (6)$$

and are normalized by $\int d\mathbf{r}[\|u_\uparrow\|^2+\|u_\downarrow\|^2-\|v_\uparrow\|^2-\|v_\downarrow\|^2]=1$. These Bogoliubov quasiparticles correspond to collective density oscillation modes around the condensate with frequency ω [24]. It is easy to see that the wave function $[v_\uparrow^*(\mathbf{r}),v_\downarrow^*(\mathbf{r}),u_\uparrow^*(\mathbf{r}),u_\downarrow^*(\mathbf{r})]^T$ is also a solution of Eq. (6), but with energy $-\hbar\omega$. This is an unphysical solution, due to the Bogoliubov transformation which enlarges the Hilbert space for quasiparticles. Physically, we should restrict it to a nonnegative mode frequency, $\omega\geqslant 0$. For the fermionic Bogoliubov transformation, we have exactly the same situation. The fermionic Bogoliubov equation has the same "particle-hole" symmetry or duality [25]. In that case, one needs to remove the particle-hole redundancy by multiplying a factor of 1/2 in the calculation of the physical quantities such as density and order parameter [25].

In harmonic traps, it is natural to use trap units; that is, to take $\hbar\omega_\perp$ as the unit for energy and the harmonic oscillator length $a_\perp=\sqrt{\hbar/(M\omega_\perp)}$ as the unit for length. This is equivalent to setting $\hbar=k_B=M=\omega_\perp=1$. The unit of interaction strength $g(N-1)$ or $g_{\uparrow\downarrow}(N-1)$ is then $\hbar\omega_\perp a_\perp^2=\hbar^2/M$. For SO coupling, we introduce an SO coupling length $a_\lambda=\hbar^2/(M\lambda_{\rm R})$ and consequently define a dimensionless SO coupling strength $\lambda_{\rm SO}=a_\perp/a_\lambda=\sqrt{(M/\hbar^3)}\lambda_{\rm R}/\sqrt{\omega_\perp}$. In an SO-coupled spin-1/2 BEC of ^{87}Rb atoms as realized recently by the NIST group [5], $\lambda_{\rm SO}$ is about 10. In the typical experiment for 2D spin-1/2 ^{87}Rb BECs [21], the interatomic interaction strengths are about $g(N-1)\approx g_{\uparrow\downarrow}(N-1)=10^2\sim 10^3(\hbar\omega_\perp a_\perp^2)$. These coupling strengths, however, can be tuned by changing the number of trapped atoms or by properly choosing the parameters of the laser fields that lead to the harmonic confinement and the SO coupling.

B. Single-particle solutions

The appearance of the half-quantum vortex state may be easily understood in the noninteracting limit [14]. In the absence of interatomic interactions, the single-particle wave function $[\phi_\uparrow(\mathbf{r}),\phi_\downarrow(\mathbf{r})]^T$ with energy ϵ is given by

$$\begin{bmatrix}\mathcal{H}_{\rm osc} & -i\lambda_{\rm R}(\partial_y+i\partial_x)\\ -i\lambda_{\rm R}(\partial_y-i\partial_x) & \mathcal{H}_{\rm osc}\end{bmatrix}\begin{bmatrix}\phi_\uparrow\\ \phi_\downarrow\end{bmatrix}=\epsilon\begin{bmatrix}\phi_\uparrow\\ \phi_\downarrow\end{bmatrix}. \quad (7)$$

In polar coordinates (ρ,φ), we have $-i(\partial_y\pm i\partial_x)=e^{\mp i\varphi}[\pm\partial/\partial\rho-(i/\rho)\partial/\partial\varphi]$. Because of the isotropic harmonic potential $V(\rho)$, the single-particle wave function has a well-defined azimuthal angular momentum $l_z=m$ and takes the form

$$\phi_m(\mathbf{r})=\begin{bmatrix}\phi_\uparrow(\rho)\\ \phi_\downarrow(\rho)e^{i\varphi}\end{bmatrix}\frac{e^{im\varphi}}{\sqrt{2\pi}}. \quad (8)$$

This state also has a well-defined total angular momentum $j_z=l_z+s_z=m+1/2$. In general, we may denote the energy spectrum as ϵ_{nm}, where $n=(0,1,2,\ldots)$ is the quantum number for the transverse (radial) direction. There is an interesting twofold degeneracy of the energy spectrum: any eigenstate $\phi(\mathbf{r})=[\phi_\uparrow(\mathbf{r}),\phi_\downarrow(\mathbf{r})]^T$ is degenerate with its time-reversal partner $\mathcal{T}\phi(\mathbf{r})\equiv(i\sigma_y\mathcal{C})\phi(\mathbf{r})=[\phi_\downarrow^*(\mathbf{r}),-\phi_\uparrow^*(\mathbf{r})]^T$. Here $\mathcal{C}$ is the complex conjugate operation. This Kramer doublet is the direct consequence of the time-reversal symmetry satisfied by the model Hamiltonian. This symmetry is preserved in the presence of interatomic interactions. As a result, we may restrict the quantum numbers m to be non-negative integers, since a negative m can always be regarded as the time-reversal partner for a state with $m\geqslant 0$.

To numerically solve the single-particle spectrum, we adopt a basis-expansion method. To this end, we first expand,

$$\phi_\uparrow(\rho)=\sum_k A_k R_{km}(\rho), \quad (9)$$

$$\phi_\downarrow(\rho)=\sum_k B_k R_{km+1}(\rho), \quad (10)$$

where

$$R_{km}=\frac{1}{a_\perp}\sqrt{\frac{2k!}{(k+|m|)!}}\left(\frac{\rho}{a_\perp}\right)^{|m|}e^{-\frac{\rho^2}{2a_\perp^2}}\mathcal{L}_k^{|m|}\left(\frac{\rho^2}{a_\perp^2}\right) \quad (11)$$

is the radial wave function of a 2D harmonic oscillator $\mathcal{H}_{\rm osc}$ with energy $(2k+\|m\|+1)\hbar\omega_\perp$, and $\mathcal{L}_k^{\|m\|}$ is the associated Legendre polynomial. Then we have the following secular matrix:

$$\begin{bmatrix}\mathcal{H}_{{\rm osc}\uparrow} & \mathcal{M}^T\\ \mathcal{M} & \mathcal{H}_{{\rm osc}\downarrow}\end{bmatrix}\begin{bmatrix}A_k\\ B_k\end{bmatrix}=\epsilon\begin{bmatrix}A_k\\ B_k\end{bmatrix}, \quad (12)$$

where the matrix elements are given by (for $m\geqslant 0$)

$$\mathcal{H}_{{\rm osc}\uparrow,kk'}=\hbar\omega_\perp[2k+m+1]\delta_{kk'},$$
$$\mathcal{H}_{{\rm osc}\downarrow,kk'}=\hbar\omega_\perp[2k+(m+1)+1]\delta_{kk'},$$
$$\mathcal{M}_{kk'}=\hbar\omega_\perp\lambda_{\rm SO}[\sqrt{k'+m+1}\delta_{kk'}+\sqrt{k'}\delta_{kk'-1}].$$

Diagonalization of the secular matrix Eq. (12) leads to the single-particle spectrum and single-particle wave functions.

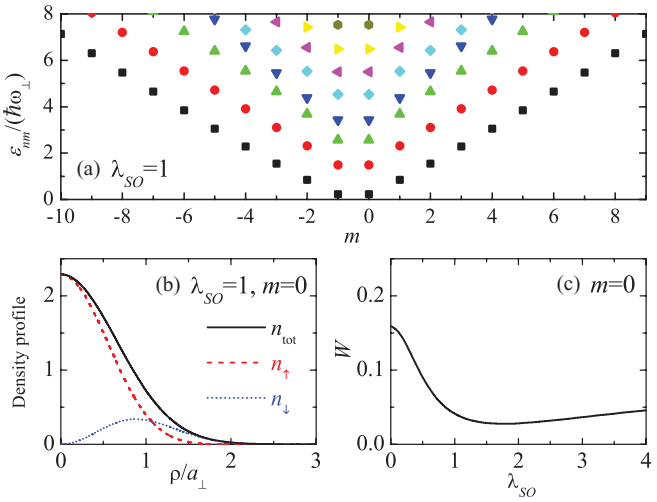

FIG. 2. (Color online) (a) Single-particle energy spectrum at $\lambda_{SO} = 1$. (b) Density profiles for the single-particle state with $m = 0$ at $\lambda_{SO} = 1$. (c) W-function for the $m = 0$ single-particle state as a function of SO-coupling strength. It is always positive at arbitrary SO-coupling strength.

In numerical calculations, it is necessary to impose a cutoff k_{max} for the radial quantum number k of the 2D harmonic oscillator. For $\lambda_{SO} \leqslant 20$, we find that $k_{max} = 256$ is sufficiently large to have an accurate energy spectrum. With this cutoff, the dimension of the secular matrix in Eq. (12) is $2k_{max} = 512$.

In Fig. 2(a), we show the single-particle energy spectrum at $\lambda_{SO} = 1$. For arbitrary SO-interaction strength, we find numerically that the doublet single-particle ground state always occurs at $m = 0$ (or $m = -1$ for its time-reversal partner state).

C. Appearance of half-quantum vortex state

The single-particle state with $m = 0$, $\phi_0(\mathbf{r}) = [\phi_\uparrow(\rho),\phi_\downarrow(\rho)e^{i\varphi}]^T/\sqrt{2\pi}$ has a half-quantum vortex configuration [14,26], because the spin-up component stays in the s state while the spin-down component is in the p state. The resulting spin texture is of skyrmion type [see Fig. 2(b) for density distributions and Sec. III B for more discussions on spin texture]. In the absence of interactions, however, there is a degenerate time-reversed state, $\mathcal{T}\phi_0(\mathbf{r}) = [\phi_\downarrow(\rho)e^{-i\varphi}, -\phi_\uparrow(\rho)]^T/\sqrt{2\pi}$, which is also a half-quantum vortex state. Therefore, in general, the ground single-particle state is a superposition of two degenerate half-quantum vortex states, $\phi_0(\mathbf{r})$ and $\mathcal{T}\phi_0(\mathbf{r})$, which takes the form $\phi_s(\mathbf{r}) = \alpha\phi_0(\mathbf{r}) + \beta\mathcal{T}\phi_0(\mathbf{r})$ or, explicitly,

$$\phi_s(\mathbf{r}) = \frac{1}{\sqrt{2\pi}}\begin{bmatrix} \alpha\phi_\uparrow(\rho) + \beta\phi_\downarrow(\rho)e^{-i\varphi} \\ \alpha\phi_\downarrow(\rho)e^{i\varphi} - \beta\phi_\uparrow(\rho) \end{bmatrix}. \tag{13}$$

Here α and β are two arbitrary complex numbers satisfying $\|\alpha\|^2 + \|\beta\|^2 = 1$.

In the presence of very weak interatomic interactions such that $g(N-1), g_{\uparrow\downarrow}(N-1) \ll \Delta\epsilon a_\perp^2$, where $\Delta\epsilon$ is the energy difference between the single-particle ground state $\phi_0(\mathbf{r})$ and the first-excited state $\phi_1(\mathbf{r})$, we may determine the superposition coefficients α and β by minimizing the GP energy, $E_{GP}[\phi_s(\mathbf{r})] = \int d\mathbf{r}\,\mathcal{H}_{GP}[\phi_s(\mathbf{r})]$. After simple algebra, we find that

$$\Delta E = E_{GP}[\phi_s(\mathbf{r})] - E_{GP}[\phi_0(\mathbf{r})], \tag{14}$$

$$= (g_{\uparrow\downarrow} - g)(N-1)|\alpha\beta|^2 W[\phi_0(\mathbf{r})], \tag{15}$$

where the W function is given by

$$W[\phi(\mathbf{r})] = \int d\mathbf{r}[(|\phi_\uparrow|^2 - |\phi_\downarrow|^2)^2 - 2\phi_\uparrow^2\phi_\downarrow^2]. \tag{16}$$

Therefore, a half-quantum vortex state is preferable if $(g_{\uparrow\downarrow} - g)W > 0$. Otherwise, an equal-weight superposition of two degenerate half-quantum vortex states with $\|\alpha\| = \|\beta\| = 1/\sqrt{2}$ will be the ground state. As shown in Fig. 2(c), the W function for $\phi_0(\mathbf{r})$ is positive for *arbitrary* SO coupling. We thus conclude that a half-quantum vortex state should appear for weak interatomic interactions provided that the interspecies interaction is larger than the intraspecies interaction $(g_{\uparrow\downarrow} > g)$.

III. DENSITY DISTRIBUTIONS AND COLLECTIVE EXCITATIONS

Let us now consider finite interatomic interactions by solving the GPE for density distributions and spin textures and the Bogoliubov equation for the collective density excitations.

A. GPE solutions of half-quantum vortex state

For the half-quantum vortex condensate state with $m = 0$, the GP equation becomes $\mathcal{L}_{GP}[\phi_\uparrow(\rho),\phi_\downarrow(\rho)] = 0$, where

$$\mathcal{L}_{GP} = \begin{bmatrix} \mathcal{H}_{s,0} + \bar{g}\phi_\uparrow^2 + \bar{g}_{\uparrow\downarrow}\phi_\downarrow^2 & \lambda_R(\partial_\rho + 1/\rho) \\ \lambda_R(-\partial_\rho) & \mathcal{H}_{s,1} + \bar{g}_{\uparrow\downarrow}\phi_\uparrow^2 + \bar{g}\phi_\downarrow^2 \end{bmatrix}. \tag{17}$$

Here, $\bar{g} \equiv g(N-1)/(2\pi)$ and $\bar{g}_{\uparrow\downarrow} \equiv g_{\uparrow\downarrow}(N-1)/(2\pi)$, while the single-particle Hamiltonian operator is

$$\mathcal{H}_{s,m} \equiv -\frac{\hbar^2}{2M}\left[\frac{\partial^2}{\partial\rho^2} + \frac{1}{\rho}\frac{\partial^2}{\partial\rho^2}\partial_\rho - \frac{m^2}{\rho^2}\right] + V(\rho) - \mu. \tag{18}$$

The numerical procedure for solving the GPE is very similar to that for single-particle states in Eq. (12). We expand $\phi_\uparrow(\rho) = \sum_k A_k R_{k0}(\rho)$ and $\phi_\downarrow(\rho) = \sum_k B_k R_{k1}(\rho)$ and obtain the secular matrix (with $m = 0$),

$$\begin{bmatrix} \mathcal{H}_{osc\uparrow} + \mathcal{I}_\uparrow & \mathcal{M}^T \\ \mathcal{M} & \mathcal{H}_{osc\downarrow} + \mathcal{I}_\downarrow \end{bmatrix}\begin{bmatrix} A_k \\ B_k \end{bmatrix} = \mu\begin{bmatrix} A_k \\ B_k \end{bmatrix}, \tag{19}$$

where

$$\mathcal{I}_{\uparrow,kk'} = \int_0^\infty \rho d\rho R_{k0}(\rho)(\bar{g}\phi_\uparrow^2 + \bar{g}_{\uparrow\downarrow}\phi_\downarrow^2)R_{k'0}(\rho), \tag{20}$$

$$\mathcal{I}_{\downarrow,kk'} = \int_0^\infty \rho d\rho R_{k1}(\rho)(\bar{g}_{\uparrow\downarrow}\phi_\uparrow^2 + \bar{g}\phi_\downarrow^2)R_{k'1}(\rho). \tag{21}$$

The chemical potential is given by the lowest eigenvalue of the secular matrix. Due to the nonlinear terms $\mathcal{I}_{\uparrow,kk'}$ and $\mathcal{I}_{\uparrow,kk'}$, we have to update the condensate wave functions and densities iteratively. To overcome the large nonlinearity, we use a simple mixing scheme by setting a small parameter $0 < \gamma < 1$ and

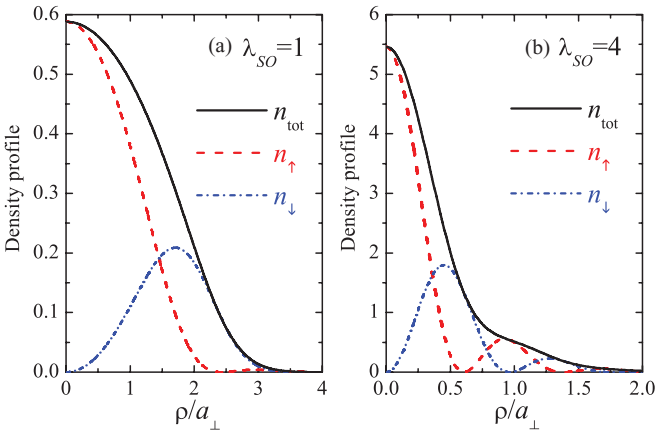

FIG. 3. (Color online) Density distributions at $\lambda_{SO} = 1$ and $g(N-1) = 40(\hbar\omega_\perp a_\perp^2)$ (a) and at $\lambda_{SO} = 4$ and $g(N-1) = \hbar\omega_\perp a_\perp^2$ (b). Here, the ratio $g_{\uparrow\downarrow}/g = 1.1$.

replacing the previous density $\phi^2_{\sigma,\text{old}}$ by $(1-\gamma)\phi^2_{\sigma,\text{old}} + \gamma\phi^2_\sigma$, where ϕ^2_σ is the density calculated in the current step [27]. The choice of γ depends on the interaction strength. It becomes smaller for larger $\bar{g}$ and $\bar{g}_{\uparrow\downarrow}$. We run this iteration until convergence is achieved within a set tolerance. We have checked that this procedure of solving the GPE is stable for interaction strengths up to $g(N-1)$, $g_{\uparrow\downarrow}(N-1) < 10^3(\hbar\omega_\perp a_\perp^2)$. For even larger nonlinearity, it seems to be impractical to expand the condensate wave function using the 2D harmonic oscillator basis. Therefore, for large interaction strengths, we use a time-splitting spectral method (TSSP) to solve the coupled GP equations and obtain the ground state by imaginary-time propagation [28,29]. For small interaction strengths, results obtained from TSSP are identical to those obtained from the basis-expansion method.

B. Density distributions and spin textures

In Fig. 3, we present the radial density distributions of the half-quantum vortex condensate state at two SO-coupling strengths: $\lambda_{SO} = 1$ and $\lambda_{SO} = 4$. The increased SO coupling leads to more oscillations in the radial direction. By comparing Fig. 3(a) with Fig. 2(b), one finds that the density distributions are flattened significantly by interatomic interactions, as anticipated. The 2D contour plot of the spin-up and spin-down density patterns of the half-quantum vortex state is shown in the inset of Fig. 1 (in phase I).

To gain more insight into the half-quantum vortex state, it is useful to calculate the spin vector

$$\mathbf{S}(\mathbf{r}) = \frac{1}{2}\frac{\Phi^\dagger\sigma\Phi}{|\Phi|^2} = \frac{1}{2}\mathbf{n}(\mathbf{r}) \tag{22}$$

and the skyrmion density

$$n_{\text{skyrmion}}(\mathbf{r}) = \frac{1}{4\pi}\mathbf{n}\cdot[\partial_x\mathbf{n}\times\partial_y\mathbf{n}]. \tag{23}$$

The skyrmion density is a measure of the winding of the spin profile. If it integrates to 1 or -1, a topological knot exists in the spin texture [30,31].

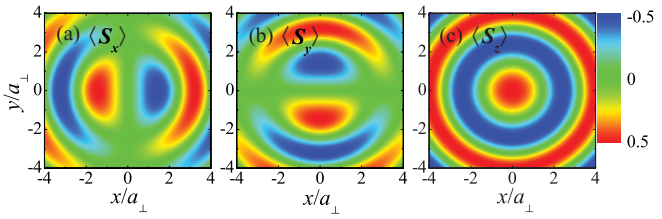

FIG. 4. (Color online) Contour plots of the three components of the spin vector $\mathbf{S}(\mathbf{r})$ at $\lambda_{SO} = 1$, $g(N-1) = 40(\hbar\omega_\perp a_\perp^2)$, and $g_{\uparrow\downarrow}/g = 1.1$.

In Fig. 4, we graph the three components of the spin vector at $\lambda_{SO} = 1$, $g(N-1) = 40(\hbar\omega_\perp a_\perp^2)$ and $g_{\uparrow\downarrow}/g = 1.1$. The transverse spin texture is shown in Figs. 5(a) and 5(b) by arrows, with arrow length representing the magnitude of the transverse spin vector (S_x, S_y) or (S_x, S_z). It is readily seen that the spin vector spirals in space to form a skyrmion-type texture. Quantitatively, this is most clearly illustrated in Figs. 5(c) and 5(d), where we plot the 2D contour and 1D radial distribution of skyrmion density, respectively. The nonzero skyrmion density oscillates between positive and negative. Moreover, the skyrmion number $\Phi = \int n_{\text{skyrmion}}(\mathbf{r})d\mathbf{r}$ is quantized to $+1$. We note that, for the time-reversal half-quantum vortex condensate state with $m = -1$, the skyrmion number is -1.

C. Solutions of Bogoliubov equations

Given the wave function of the half-quantum vortex state, $[\phi_\uparrow(\rho), \phi_\downarrow(\rho)e^{i\varphi}]^T/\sqrt{2\pi}$, we now turn to consider its collective excitations, as described by the coupled Bogoliubov equations (6). As a result of rotational symmetry, it is easy to see that the Bogoliubov wave functions have a good azimuthal quantum number m and hence can be written as

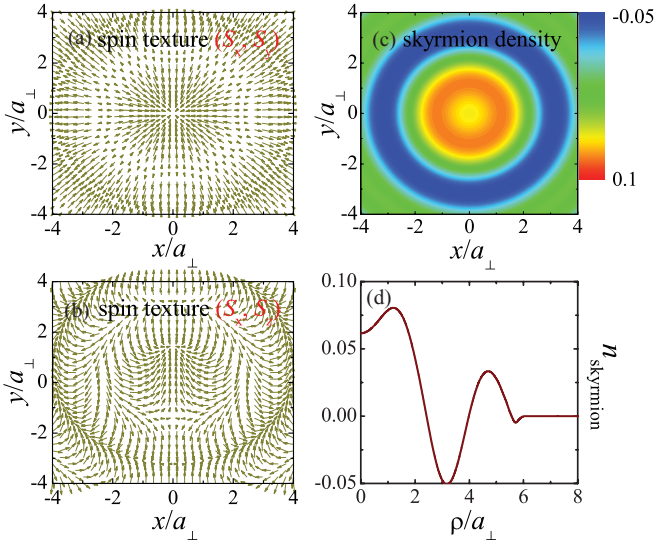

FIG. 5. (Color online) (a) and (b): Two-dimensional vector plot of the transverse spin vector (S_x, S_y) and (S_x, S_z) at $\lambda_{SO} = 1$, $g(N-1) = 40(\hbar\omega_\perp a_\perp^2)$, and $g_{\uparrow\downarrow}/g = 1.1$. The length of the arrows gives the magnitude of (S_x, S_y) or (S_x, S_z). The corresponding skyrmion density $n_{\text{skyrmion}}(\mathbf{r})$ is plotted in (c) and (d).

$[u_\uparrow(\rho),u_\downarrow(\rho)e^{i\varphi},v_\uparrow(\rho),v_\downarrow(\rho)e^{-i\varphi}]^T e^{im\varphi}/\sqrt{2\pi}$. Therefore, we have

$$\mathcal{H}_{\rm Bog}\begin{bmatrix} u_\uparrow(\rho) \\ u_\downarrow(\rho) \\ v_\uparrow(\rho) \\ v_\downarrow(\rho) \end{bmatrix} = \hbar\omega \begin{bmatrix} +u_\uparrow(\rho) \\ +u_\downarrow(\rho) \\ -v_\uparrow(\rho) \\ -v_\downarrow(\rho) \end{bmatrix}, \tag{24}$$

where

$$\mathcal{H}_{\rm Bog} = \begin{bmatrix} \mathcal{L}_m + \mathcal{U} & \mathcal{U} \\ \mathcal{U} & \mathcal{L}_{-m} + \mathcal{U} \end{bmatrix}, \tag{25}$$

with

$$\mathcal{L}_m = \begin{bmatrix} \mathcal{H}_{s,m} + \bar{g}\phi_\uparrow^2 + \bar{g}_{\uparrow\downarrow}\phi_\downarrow^2 & \lambda_{\rm R}\left[\partial_\rho + (m+1)/\rho\right] \\ \lambda_{\rm R}(-\partial_\rho + m/\rho) & \mathcal{H}_{s,m+1} + \bar{g}_{\uparrow\downarrow}\phi_\uparrow^2 + \bar{g}\phi_\downarrow^2 \end{bmatrix}, \tag{26}$$

and

$$\mathcal{U} = \begin{bmatrix} \bar{g}\phi_\uparrow^2 & \bar{g}_{\uparrow\downarrow}\phi_\uparrow\phi_\downarrow \\ \bar{g}_{\uparrow\downarrow}\phi_\uparrow\phi_\downarrow & \bar{g}\phi_\downarrow^2 \end{bmatrix}. \tag{27}$$

To solve the Bogoliubov equation, as before we expand the wave functions using a 2D harmonic oscillator basis,

$$u_\uparrow(\rho) = \sum_k a_k R_{km}(\rho), \tag{28}$$

$$u_\downarrow(\rho) = \sum_k b_k R_{km+1}(\rho), \tag{29}$$

$$v_\uparrow(\rho) = \sum_k c_k R_{km}(\rho), \tag{30}$$

$$v_\downarrow(\rho) = \sum_k d_k R_{km-1}(\rho). \tag{31}$$

This leads to a secular matrix of $\mathcal{H}_{\rm Bog}$, whose elements can be calculated directly using the 2D harmonic oscillator basis. We note that, to obtain the Bogoliubov quasiparticles, we cannot diagonalize the secular matrix directly, because of the minus sign before $v_\uparrow(\rho)$ and $v_\downarrow(\rho)$ on the right-hand side of Eq. (24). To remove the minus sign, we may multiply a matrix Diag$\{+1,+1,-1,-1\}$ on both sides of Eq. (24). Therefore, we should diagonalize a *nonsymmetric* matrix Diag$\{+1,+1,-1,-1\}\mathcal{H}_{\rm Bog}$ and normalize the quasiparticle wave functions according to

$$\int_0^\infty \rho d\rho[u_\uparrow^2 + u_\downarrow^2 - v_\uparrow^2 - v_\downarrow^2] = 1. \tag{32}$$

The number of resulting eigenvalues is two times the number that we want, since the Bogoliubov transformation enlarges the Hilbert space for quasiparticles. As we mentioned earlier, there are two branches of eigenvalues, one positive and the other negative, as a result of the "particle-hole" duality between the solution $[u_\uparrow(\mathbf{r}),u_\downarrow(\mathbf{r}),v_\uparrow(\mathbf{r}),v_\downarrow(\mathbf{r})]^T$ (with energy $+\hbar\omega$) and $[v_\uparrow^*(\mathbf{r}),v_\downarrow^*(\mathbf{r}),u_\uparrow^*(\mathbf{r}),u_\downarrow^*(\mathbf{r})]^T$ (with energy $-\hbar\omega$). We should take the positive branch, since the Bogoliubov quasiparticle corresponds to the collective oscillation of the cloud and should have the positive oscillation frequency. Note that, because of the "particle-hole" duality, in our case with rotational symmetry, the Bogoliubov quasiparticles at negative azimuthal quantum number m may be obtained from the negative energy branch of the solution with $m > 0$.

1. Breathing modes

In the case of the breathing mode ($m = 0$), where

$$\mathcal{H}_{\rm Bog} = \begin{bmatrix} \mathcal{L}_{\rm GP} + \mathcal{U} & \mathcal{U} \\ \mathcal{U} & \mathcal{L}_{\rm GP} + \mathcal{U} \end{bmatrix}, \tag{33}$$

there is an alternative way to solve the Bogoliubov equation, following Hutchinson, Zaremba, and Griffin (HZG) [32]. By denoting collectively $u = [u_\uparrow(\rho),u_\downarrow(\rho)]$ and $v = [v_\uparrow(\rho),v_\downarrow(\rho)]$, we have

$$(\mathcal{L}_{\rm GP} + 2\mathcal{U})(u+v) = \hbar\omega(u-v), \tag{34}$$

$$\mathcal{L}_{\rm GP}(u-v) = \hbar\omega(u+v). \tag{35}$$

Let us now expand the wave functions $u \pm v$ in terms of the eigenfunctions ψ_α of $\mathcal{L}_{\rm GP}$ with energy ϵ_α (i.e., $\mathcal{L}_{\rm GP}\psi_\alpha = \epsilon_\alpha\psi_\alpha$):

$$u - v = \sum_{\alpha\neq 0} \frac{c_\alpha}{\epsilon_\alpha^{1/2}}\psi_\alpha, \tag{36}$$

$$u + v = \sum_{\alpha\neq 0} \frac{\epsilon_\alpha^{1/2} c_\alpha}{\hbar\omega}\psi_\alpha. \tag{37}$$

Here, the lowest eigenstate of $\mathcal{L}_{\rm GP}$ with zero energy should be removed, because it simply corresponds to the condensate mode. It is easy to see that $(\mathcal{L}_{\rm GP} + 2\mathcal{U})\mathcal{L}_{\rm GP}(u-v) = (\hbar\omega)^2(u-v)$ and $\mathcal{L}_{\rm GP}(\mathcal{L}_{\rm GP} + 2\mathcal{U})(u+v) = (\hbar\omega)^2(u+v)$. Inserting the expansion of $u-v$ or $u+v$, one finds the secular equation

$$\sum_\beta \left\{\epsilon_\alpha^2\delta_{\alpha\beta} + 2\epsilon_\alpha^{1/2}\mathcal{U}_{\alpha\beta}\epsilon_\beta^{1/2}\right\}c_\beta = (\hbar\omega)^2 c_\alpha, \tag{38}$$

where

$$\mathcal{U}_{\alpha\beta} = \int_0^\infty \rho d\rho \psi_\alpha^\dagger(\rho)\mathcal{U}\psi_\beta(\rho). \tag{39}$$

By diagonalizing the secular matrix, one obtains the mode frequency ω and the coefficients c_α. The latter should be normalized as $\sum_\alpha c_\alpha^2 = \hbar\omega$, in accord with the normalization condition for u and v.

We have numerically checked that the HZG solution leads to exactly the same result as the direct diagonalization of the nonsymmetric matrix Diag$\{+1,+1,-1,-1\}\mathcal{H}_{\rm Bog}$, if we discard the zero-frequency condensate mode in the latter method.

D. Collective excitations

In Fig. 6, we graph the breathing ($m = 0$) and the dipole mode ($m = \pm 1$) frequencies as a function of the interaction strength. With increasing interaction, the mode frequency decreases and appears to saturate at sufficiently large interactions. This may be anticipated from the point of view of two-fluid hydrodynamic behavior in the Thomas-Fermi regime. In Fig. 7, we report the dependence of the mode frequencies on SO coupling. In the absence of SO coupling, the breathing mode with $\omega = 2\omega_\perp$ and the dipole mode with $\omega = \omega_\perp$ are the exact solutions of quantum many-body systems in a harmonic trap.

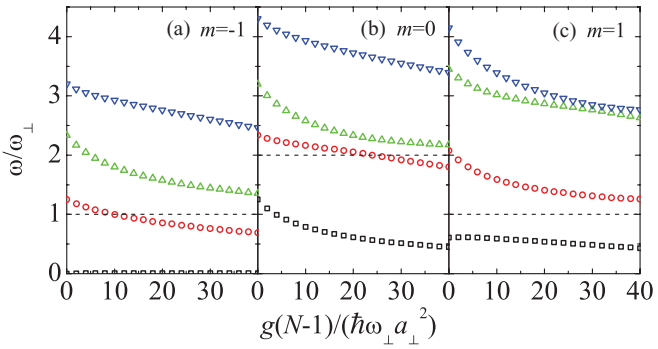

FIG. 6. (Color online) Mode frequency of breathing ($m = 0$) and dipole ($m = \pm 1$) modes as a function of interaction strength at fixed SO coupling $\lambda_{SO} = 1$ and at $g_{\uparrow\downarrow} = 1.1g$.

At a finite SO coupling we find that these two solutions are no longer exact. The relative deviations of the breathing mode and dipole mode at $\lambda_{SO} = 1$ are about 10% and 30%, respectively, from the exact solution of $\omega = 2\omega_\perp$ and $\omega = \omega_\perp$ in the absence of SO coupling.

In Fig. 8, we plot the Bogoliubov wave functions of the lowest four breathing modes at $\lambda_{SO} = 1$, $g(N-1) = 40(\hbar\omega_\perp a_\perp^2)$, and $g_{\uparrow\downarrow} = 1.1g$. We find that the density response is mainly carried by $u_\uparrow(\rho)$ and $u_\downarrow(\rho)$ components. With increasing mode frequency, more nodes appear in $u_\uparrow(\rho)$ and $u_\downarrow(\rho)$. In contrast, the response in $v_\uparrow(\rho)$ and $v_\downarrow(\rho)$ is relatively weak, and the curve shape is nearly unchanged as the mode frequency increases.

E. Dynamical Calculations

To investigate the dynamical properties of the system, we have also performed direct numerical simulations of the system by real-time propagation of the ground state under perturbation. To do this, we first obtain the ground state by solving the coupled GP equations in Eq. (3) using the TSSP technique [33]. The half-quantum vortex ground state is perturbed in various ways. We observe that the mode frequencies obtained by dynamical simulation agree well with those obtained by solving the Bogoliubov equations (shown in Fig. 6).

Breathing mode analysis, $m = 0$. We excite the monopole mode by weak relaxation of the trapping frequency at time

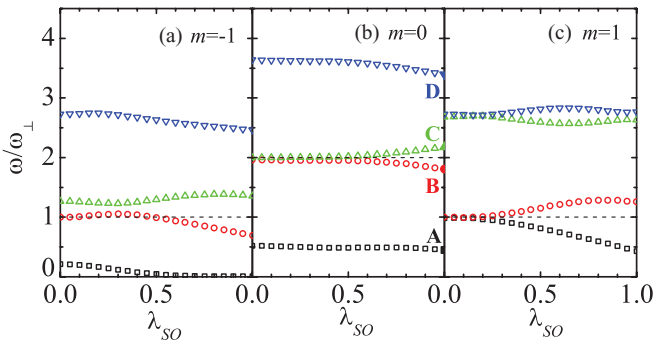

FIG. 7. (Color online) Mode frequency of breathing ($m = 0$) and dipole ($m = \pm 1$) modes as a function of SO coupling at fixed interaction strength $g(N-1) = 40(\hbar\omega_\perp a_\perp^2)$ and at $g_{\uparrow\downarrow} = 1.1g$.

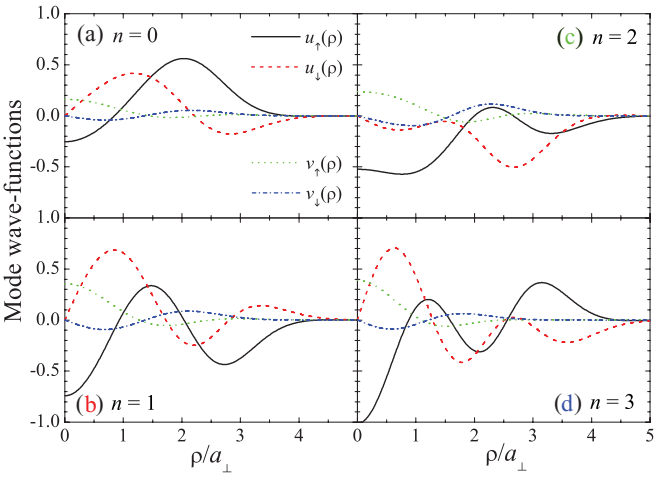

FIG. 8. (Color online) Bogoliubov wave functions of the lowest four breathing modes at $\lambda_{SO} = 1$, $g(N-1) = 40(\hbar\omega_\perp a_\perp^2)$, and $g_{\uparrow\downarrow} = 1.1g$. The mode frequencies are indicated in Fig. 7(b) by solid symbols.

$t = 0$ and by letting the system propagate in time. As the breathing mode excitation is isotropic in x-y space, it is sufficient to observe the dynamic response of the collective coordinate along one axis, say, the x axis. Here, we pick the mean square of the center-of-mass coordinate as the quantity of interest:

$$\langle x^2\rangle_\sigma = \frac{\int |\phi_\sigma|^2 x^2 dxdy}{\int |\phi_\sigma|^2 dxdy},$$

where $\sigma = \uparrow, \downarrow$-spin components. In Figs. 9(a) and 9(b), we plot the time response of $\langle x^2(t)\rangle_\sigma$ for a typical parameter set. In Figs. 9(c) and 9(d), we show the corresponding frequency response by plotting the single-sided amplitude spectrum $|\langle x^2(\omega)\rangle|_\sigma$, which is just the Fourier transforms of $\langle x^2(t)\rangle_\sigma$.

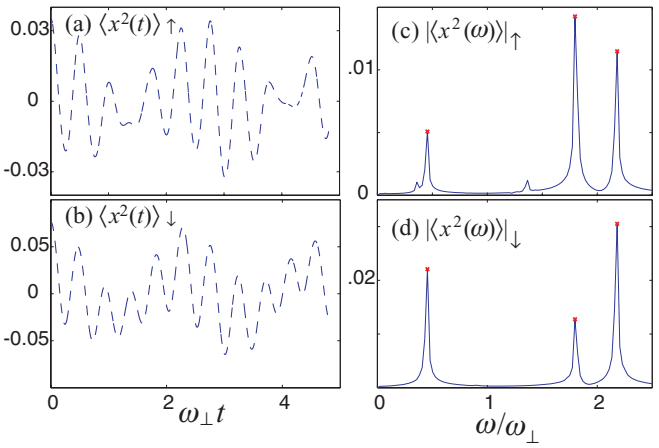

FIG. 9. (Color online) (a) and (b): Dynamic response of the mean square of the center-of-mass coordinate in x direction of $\uparrow$- and $\downarrow$-spin components, respectively. We have shifted the curves by subtracting the time-averaged $\langle x^2(t)\rangle_\sigma$. Without this shift, the Fourier spectrum as shown in (c) and (d) is dominated by a large peak at $\omega = 0$. (c) and (d): Corresponding single-sided amplitude spectrum of the collective coordinate. Parameters used: $\lambda_{SO} = 1.0$, $g(N-1) = 40(\hbar\omega_\perp a_\perp^2)$, $g_{\uparrow\downarrow}/g = 1.1$.

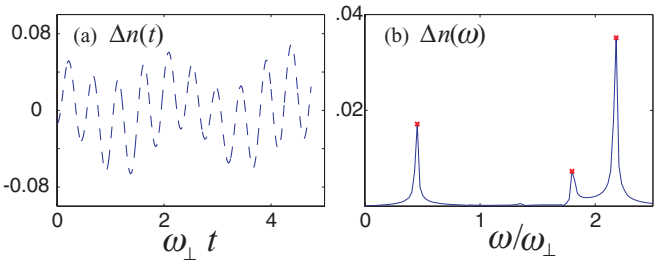

FIG. 10. (Color online) (a) Dynamic response and (b) single-sided amplitude spectrum of population difference Δn for the same parameter set used in Fig. 9.

We observe frequency peaks at $\omega/\omega_\perp \simeq 0.46$, 1.8, 2.18, and 3.40 (not shown). We note that these values exactly match the mode frequencies obtained for this parameter set by solving the Bogoliubov equations, shown in Fig. 6(b).

Dynamical calculations also reveal the coupling between the center-of-mass motion and the internal spin degrees of freedom, a trademark signature of spin-orbit coupled systems. We shall now discuss the dynamic response of the population difference $\Delta n = \int d\mathbf{r}\,(|\phi_\uparrow|^2 - |\phi_\downarrow|^2)$. In Fig. 10(a), we plot the time response of $\Delta n(t)$ for the same parameter set mentioned in Fig. 9. In Fig. 10(b), we show the corresponding frequency response by plotting the single-sided amplitude spectrum $|\Delta n(\omega)|$. We observe frequency peaks at $\omega/\omega_\perp \simeq$ 0.46, 1.8, 2.18, and 3.40 (not shown), exactly matching the mode frequencies obtained in Fig. 9. This analysis clearly shows that the population transfer between the two spin components shares a similar dynamic response with the collective motional coordinate. In this aspect, the response of Δn in a spin-orbit-coupled spinor BEC (shown here) is similar to the effects observed in multicomponent condensates, in the presence of internal Josephson coupling [34].

Dipole mode analysis, $m = \pm 1$. We excite the dipole modes by displacing the trap in the x direction by a small amount at time $t = 0$ and by letting the system propagate in time. We observe the dynamic response of the center-of-mass coordinate in the x direction:

$$\langle x\rangle_\sigma = \frac{\int |\phi_\sigma|^2 x\,dx\,dy}{\int |\phi_\sigma|^2\,dx\,dy}.$$

In Figs. 11(a) and 11(b), we plot the time response of this collective coordinate in the x direction of ↑- and ↓-spin components for a typical parameter set. In Figs. 11(c) and 11(d), we show the corresponding frequency response by plotting the single-sided amplitude spectrum $|\langle x(\omega)\rangle|_\sigma$. We observe frequency peaks at $\omega/\omega_\perp \simeq 0.05$, 0.43, 0.70, 1.25, and 1.34 (shown), and at 2.5, 2.64, and 2.76 (not shown). We note that these values also agree with the mode frequencies obtained for this parameter set by solving the Bogoliubov equations, shown in Figs. 6(a) and 6(c).

In the inset of Fig. 11(a), we show the dynamics of the center-of-mass coordinate. It is important to note that, even though the trap is displaced only in the x direction, we also observe a similar dynamic response in the y direction of both spin components (only ↑-spin component shown). This behavior occurs due to the vorticity induced by the spin-orbit coupling: the vortex state experiences a Magnus force that is perpendicular to its motion. Hence a displacement in the x direction induces a motion along the y direction. Furthermore, the trace of the center of mass and its magnitude are affected by the strength of the interparticle interactions and the spin-orbit-coupling–induced population transfer, as observed in the case of the breathing mode excitation, between the ↑- and ↓-spin components.

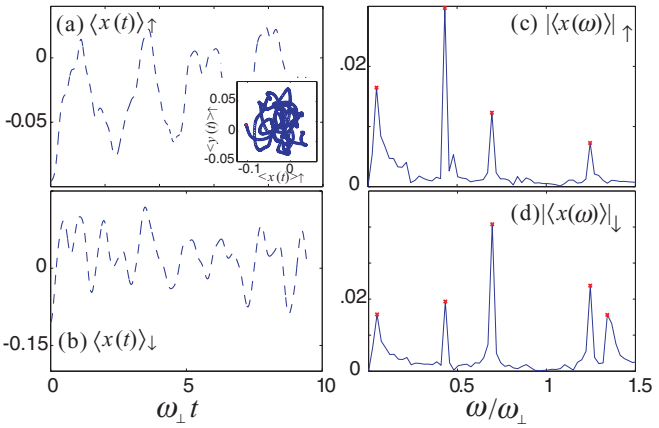

FIG. 11. (Color online) Parameters used: $\lambda_{SO} = 1.0$, $g(N-1) = 40(\hbar\omega_\perp a_\perp^2)$, $g_{\uparrow\downarrow} = 1.1\,g$. (a) and (b): Dynamic response of center-of-mass coordinate in x direction of ↑- and ↓-spin components, respectively. The inset in (a) shows the dynamics of the center-of-mass coordinate over 12 trap periods. The filled (red) marker denotes the initial position. (c) and (d): Corresponding single-sided amplitude spectrum of the collective coordinate.

IV. INSTABILITY ANALYSIS AND PHASE DIAGRAM

We are now ready to analyze the parameter space for the existence of a half-quantum vortex state. It becomes unstable with respect to increasing interaction strength or decreasing coupling ratio $g_{\uparrow\downarrow}/g$. The instability can be explained either by energy considerations and by the softening of collective density modes.

A. Superposition instability

As mentioned earlier, for any half-quantum vortex state, $\phi(\mathbf{r}) = [\phi_\uparrow(\rho), \phi_\downarrow(\rho)e^{i\varphi}]^T/\sqrt{2\pi}$, there is a degenerate time-reversal partner state, $\mathcal{T}\phi(\mathbf{r}) = [\phi_\downarrow(\rho)e^{-i\varphi}, -\phi_\uparrow(\rho)]^T/\sqrt{2\pi}$. This leads to an instability for the half-quantum vortex state with respect to a superposition state, which, with equal weight, takes the form

$$\phi_s(\mathbf{r}) = \frac{1}{\sqrt{4\pi}}\begin{bmatrix} \phi_\uparrow(\rho) + \phi_\downarrow(\rho)e^{-i(\varphi-\varphi_0)} \\ \phi_\downarrow(\rho)e^{i(\varphi-\varphi_0)} - \phi_\uparrow(\rho) \end{bmatrix}. \tag{40}$$

Here, φ_0 is an arbitrary azimuthal angle. The energy difference between the superposition state and the half-quantum vortex state is given by

$$\Delta E_{GP} = \frac{(g_{\uparrow\downarrow} - g)(N-1)}{4} W[\phi(\mathbf{r})]. \tag{41}$$

Therefore, if $W[\phi(\mathbf{r})] > 0$, the half-quantum vortex state is stable only when $g < g_{\uparrow\downarrow}$.

In Figs. 12(a) and 12(b), we check the W function of the half-quantum vortex state in the presence of interatomic

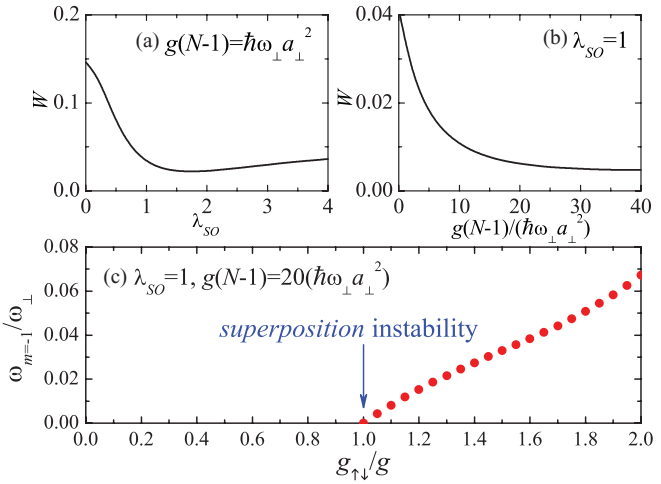

FIG. 12. (Color online) (a) W function as a function of SO coupling at $g(N-1)=\hbar\omega_\perp a_\perp^2$ and $g_{\uparrow\downarrow}=1.1g$. (b) W function as a function of interaction strength at $\lambda_{\rm SO}=1$ and $g_{\uparrow\downarrow}=1.1g$. (c) Instability of the lowest dipole mode frequency $\omega_{m=-1}$ with decreasing $g_{\uparrow\downarrow}/g$ at $\lambda_{\rm SO}=1$ and $g(N-1)=20(\hbar\omega_\perp a_\perp^2)$.

interactions. It always appears to be positive, although the interactions tend to decrease its absolute magnitude. Hence, there must be a quantum phase transition occurring at the isotropic point $g=g_{\uparrow\downarrow}$. Once $g>g_{\uparrow\downarrow}$, a superposition state with density pattern

$$n_{\uparrow,\downarrow}=\frac{1}{2\pi}\left[\frac{\phi_\uparrow^2+\phi_\downarrow^2}{2}\pm\phi_\uparrow\phi_\downarrow\cos(\varphi-\varphi_0)\right] \tag{42}$$

becomes preferable. The 2D contour plot of this density pattern with $\varphi_0=0$ is schematically shown in the inset of Fig. 1 (in the phase II A).

In general, in passing through the quantum phase transition point, we observe the softening of a particular mode frequency. As the superposition state involves a time-reversed state with angular momentum $m=-1$, the lowest dipole mode with $m=-1$ can become unstable. In Fig. 12(c), we plot the lowest dipole mode frequency $\omega_{m=-1}$ as a function of $g_{\uparrow\downarrow}/g$ at $\lambda_{\rm SO}=1$ and $g(N-1)=20(\hbar\omega_\perp a_\perp^2)$. Indeed, with decreasing $g_{\uparrow\downarrow}/g$, the mode frequency $\omega_{m=-1}$ decreases and approaches to zero exactly at the phase transition point.

B. Instability with respect to high-order angular momentum components

There is another instability for the half-quantum vortex state, which occurs with increasing interatomic interaction strength. With sufficiently large interactions, we anticipate that the state with high-order azimuthal angular momentum will energetically become favorable. For example, let us consider a condensate state with an azimuthal angular momentum $m=1$ (the 3/2-quantum vortex state), which has the form

$$\phi_{m=1}(\mathbf{r})=\frac{1}{\sqrt{2\pi}}\begin{bmatrix}\phi_\uparrow(\rho)e^{i\varphi}\\ \phi_\downarrow(\rho)e^{i2\varphi}\end{bmatrix}. \tag{43}$$

The GP energy of this state can be obtained by solving the GPE equation as before, except that we need to take $R_{k1}(\rho)$ and $R_{k2}(\rho)$ as the expansion functions for $\phi_\uparrow(\rho)$ and $\phi_\downarrow(\rho)$, respectively. Its degenerate time-reversal partner state has an azimuthal angular momentum $m=-2$.

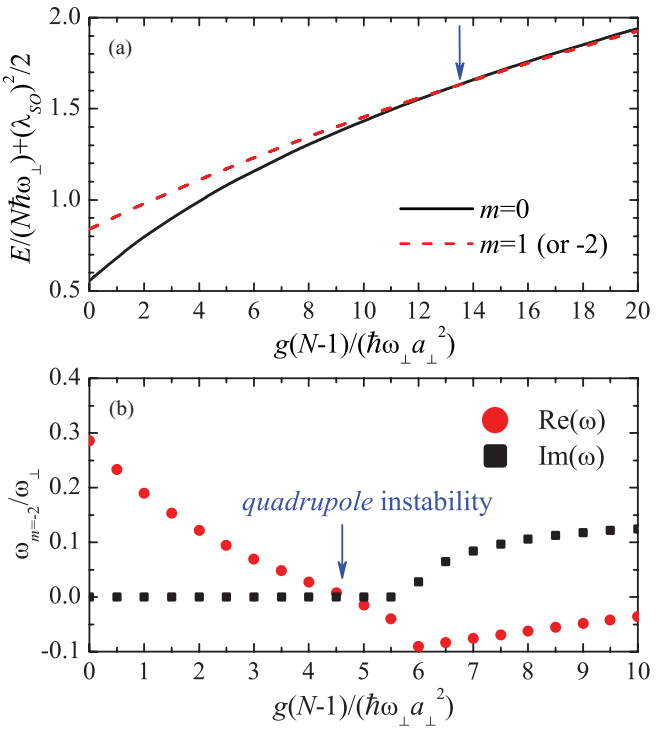

FIG. 13. (Color online) (a) GP energy of the 3/2-quantum vortex state $\phi_{m=1}(\mathbf{r})$ and of the half-quantum vortex state $\phi_{m=0}(\mathbf{r})$ as a function of interaction strength at $\lambda_{\rm SO}=2$ and $g_{\uparrow\downarrow}/g=1.1$. Beyond a critical interaction strength as indicated by an arrow, $\phi_{m=1}(\mathbf{r})$ becomes energetically favorable. (b) The corresponding lowest quadrupole mode frequency $\omega_{m=-2}$. It becomes unstable beyond a threshold g_c.

It is easy to see from Fig. 13(a) that, beyond a critical interaction strength, the condensate state with $m=1$, $\phi_{m=1}(\mathbf{r})$, is lower in energy than the half-quantum vortex state, $\phi_{m=0}(\mathbf{r})$. We note, however, that the critical interaction strength determined in this way is not accurate, as a superposition state of $\phi_{m=0}(\mathbf{r})$ and $\phi_{m=1}(\mathbf{r})$ may already become energetically more preferable than $\phi_{m=1}(\mathbf{r})$ at a smaller interaction strength.

An accurate determination of the threshold could be obtained by monitoring the instability in a particular collective mode. As the condensate state has a well-defined parity, we find that the instability occurs in the lowest quadrupole mode with $m=-2$. In Fig. 13(b), we graph the lowest quadrupole mode frequency $\omega_{m=-2}$ as a function of the interaction strength. As the interaction increases, the real part of mode frequency decreases to zero and the imaginary part becomes positive, indicating clearly that this mode will exponentially grow if the condensate is initially in the half-quantum vortex configuration. The condensate then starts to involve high-order angular momentum components. The critical interaction strength g_c can be determined simply from the softening of the mode frequency [i.e., $\omega_{m=-2}(g=g_c)=0$].

In Fig. 14, we graph the critical interacting strength as a function of SO coupling at $g_{\uparrow\downarrow}=g$ and $g_{\uparrow\downarrow}=2g$. The solid line at the isotropic point $g_{\uparrow\downarrow}/g$ has been recently calculated

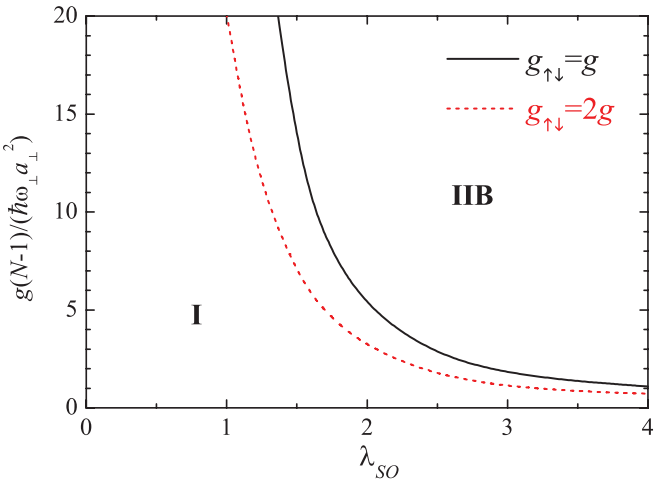

FIG. 14. (Color online) Phase diagram at $g_{\uparrow\downarrow} = g$ and $g_{\uparrow\downarrow} = 2g$. The critical interaction strength has been shown as a function of SO coupling.

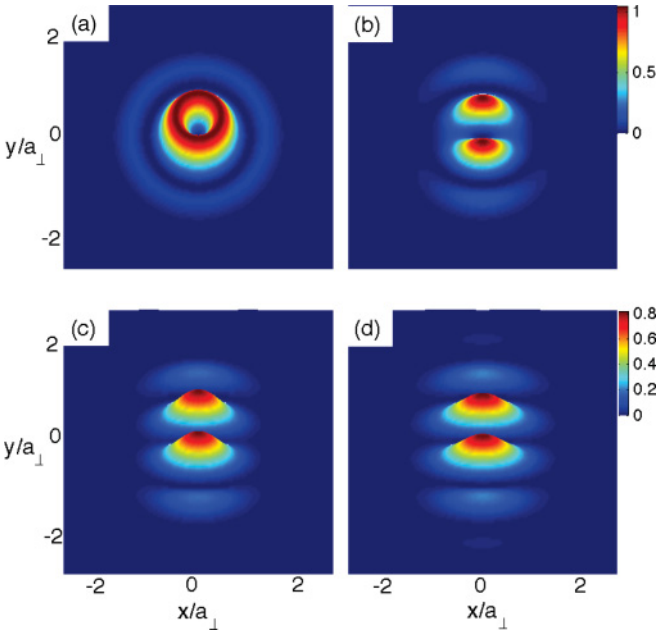

FIG. 15. (Color online) Plot of the ground state density profiles of ↓-spin component for the parameter set: $g(N-1) = 0.1(\hbar\omega_\perp a_\perp^2)$, $g_{\uparrow\downarrow}/g = 1.1$, $\lambda_x = 4.0$, with varying ratios of λ_x/λ_y. (a) Isotropic case: $\lambda_x/\lambda_y = 1.0$, (b) $\lambda_x/\lambda_y = 1.01$, (c) $\lambda_x/\lambda_y = 1.05$, (d) $\lambda_x/\lambda_y = 1.1$. Viewing angle is slightly tilted for aesthetic purposes.

by Xiang-Fa Zhou and Congjun Wu by using an imaginary time evolution method [14]. Our results are in excellent agreement with theirs. We find that, at smaller SO couplings, the critical interaction strength decreases rapidly with increasing $g_{\uparrow\downarrow}/g$.

C. Instability against anisotropy in SO-coupling strength

So far we have focused our attention on the half-quantum vortex state in an isotropic 2D harmonic trap subject to an isotropic Rashba SO coupling. Here we discuss the effect of anisotropy in the SO-coupling strength λ_R on the stability of the half-quantum vortex state. The effect of *trap* anisotropy will be discussed in the next subsection. In the context of ultracold gases, anisotropic Rashba spin-orbit coupling was first discussed in Ref. [6] and the coupled GP equations were solved for a many-body system in the absence of the trap and in the restricted scenario where $g_{\uparrow\downarrow} = g$.

Here, we move beyond these restrictions and discuss the ground state of the system. We write the SO-coupling term in the form $\mathcal{V}_{SO} = -i(\lambda_y\hat{\sigma}_x\partial_y - \lambda_x\hat{\sigma}_y\partial_x)$, where λ_x and λ_y are SO-coupling strengths in the two perpendicular directions. By including this SO-coupling term and solving the coupled GP equations under the Hamiltonian as given in Eq. (3) using the TSSP technique, we obtain the ground-state wave function at various values of anisotropy in SO coupling represented by λ_x/λ_y. In Fig. 15, we plot the corresponding ground-state density profiles of ↓-spin component for an SO coupling strength of $\lambda_x = 4.0$ and for various values of λ_x/λ_y.

We see from Fig. 15(a) that the half-quantum vortex state is indeed the ground state [already mentioned in Fig. 1(b)] for the parameter set: $g(N-1) = 0.1(\hbar\omega_\perp a_\perp^2)$, $g_{\uparrow\downarrow}/g = 1.1$, $\lambda_x = 4.0$, and $\lambda_x/\lambda_y = 1.0$. We shall now analyze the pattern of density profile changes, as the anisotropy in SO-coupling strength is varied. This is shown in Figs. 15(b)–15(d). It is evident from the density distributions in Fig. 15 that the half-quantum vortex state is unstable even against a small anisotropy in the SO-coupling strength. Adopting a similar method to that presented in Ref. [35], we analyze this systematically by expanding the wave function of the down-spin ↓-component in an orthogonal basis set of the form $\Phi_\downarrow(\rho) = \Sigma_n\, f_n(\rho)\, e^{i(2n+1)\varphi}$, where n measures the vorticity and $f_n(\rho)$ absorbs the nth mode's contribution in the radial direction. We quantify the weights of the wave function in the nth mode by computing $a_n = \int d\rho\, |f_n(\rho)|^2$. In Fig. 16, we plot the weights a_n relative to a_0, as computed for a half-quantum vortex state with $\lambda_x/\lambda_y = 1.0$. As we would expect, for this

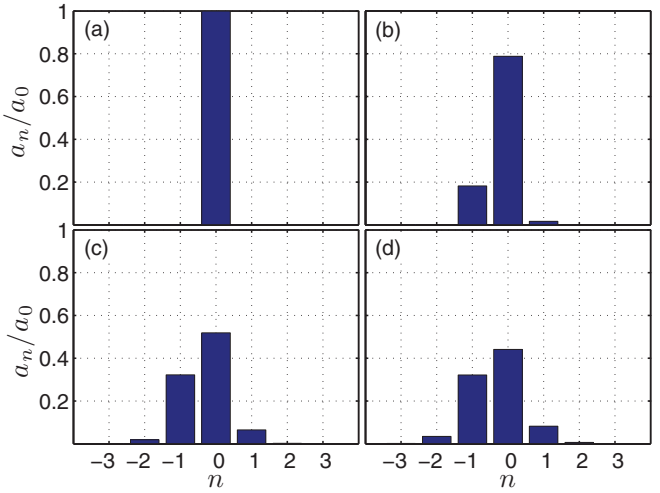

FIG. 16. (Color online) Plot of the weights of the ground-state wave function of ↓-spin component—corresponding to the density profiles in Fig. 15—in the nth mode. The weights are normalized with respect to a_0 computed for a half-quantum vortex state with $\lambda_x/\lambda_y = 1.0$. (a) Isotropic case: $\lambda_x/\lambda_y = 1.0$, (b) $\lambda_x/\lambda_y = 1.01$, (c) $\lambda_x/\lambda_y = 1.05$, (d) $\lambda_x/\lambda_y = 1.1$.

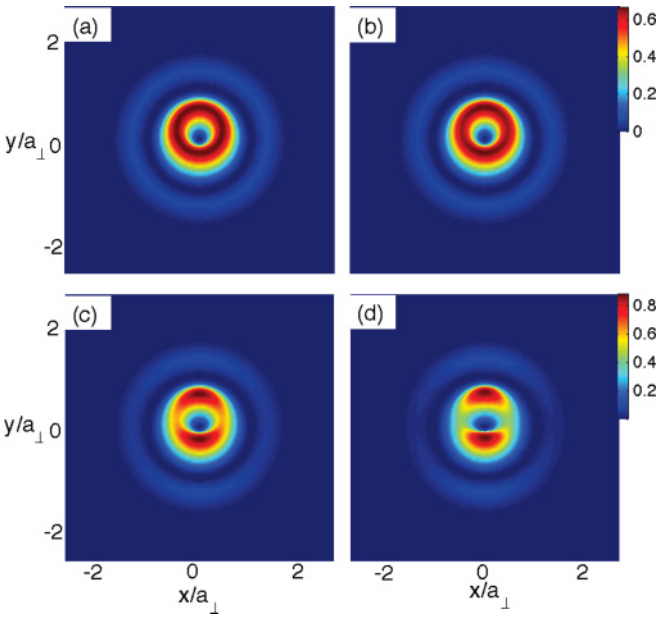

FIG. 17. (Color online) Plot of ground-state density profiles of ↓-spin component for the parameter set: $\lambda_{SO} = 4.0$, $g(N-1) = 0.1(\hbar\omega_\perp a_\perp^2)$, $g_{\uparrow\downarrow}/g = 1.1$, but with varying ratios of $f_y = \omega_y/\omega_x$. (a) Isotropic case: $f_y = 1.0$, (b) $f_y = 1.01$, (c) $f_y = 1.05$, (d) $f_y = 1.1$. Viewing angle is slightly tilted for aesthetic purposes.

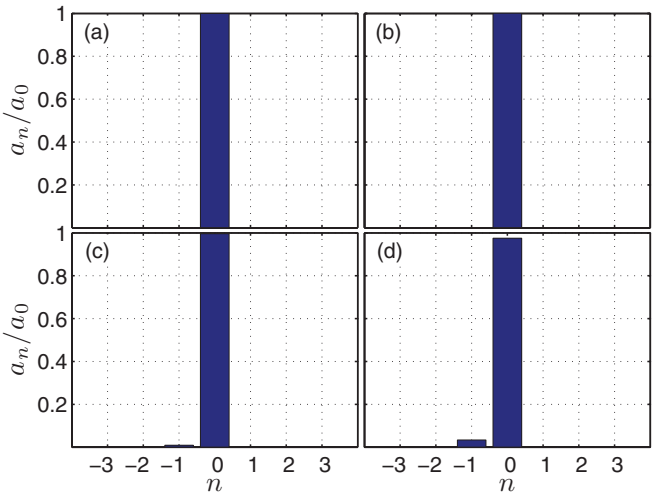

FIG. 18. (Color online) Plot of the weights of ground-state wave function of ↓-spin component—corresponding to the density profiles in Fig. 17—in the nth mode. The weights are normalized with respect to a_0 computed for half-quantum vortex state with $f_y = 1.0$. (a) Isotropic case: $f_y = 1.0$, (b) $f_y = 1.01$, (c) $f_y = 1.05$, (d) $f_y = 1.1$.

isotropic case, $a_0 = 1$ and $a_n = 0$ for $n \neq 0$. As the anisotropy in the SO-coupling strength increases, more and more $n \neq 0$ components become mixed into the ground state.

We note that, due to the sensitivity of the half-quantum vortex state with respect to the anisotropy in the SO-coupling strength, to observe such a state therefore requires a highly symmetric Rashba spin-orbit coupling in future experiments.

D. Instability to anisotropy in trap potential

Now we examine the effect of anisotropy in the trapping potential, but with isotropic SO coupling, on the stability of half-quantum vortex state. We write the trapping potential in the form $V(x,y) = M(\omega_x^2 x^2 + \omega_y^2 y^2)/2 = M\omega_\perp^2(x^2 + f_y^2 y^2)/2$, where $\omega_x = \omega_\perp, \omega_y = f_y\omega_\perp$ are trapping frequencies in x- and y directions respectively. We again obtain the ground-state wave functions at various values of f_y by solving the coupled GP equations using the TSSP technique. In Fig. 17, we plot the corresponding ground-state density profiles of the ↓-spin component for an SO-coupling strength of $\lambda_{SO} = 4.0$ and for various values of trap anisotropy ranging from 0 to 10%.

We see from Fig. 17(a) that the half-quantum vortex state is indeed the ground state [already mentioned in Fig. 15(a)] for the parameter set: $\lambda_{SO} = 4.0$, $g(N-1) = 0.1(\hbar\omega_\perp a_\perp^2)$, $g_{\uparrow\downarrow}/g = 1.1$. We shall now analyze the pattern in which the density profile changes depending on the trap anisotropy, as shown in Figs. 17(b)–17(d). It is evident from the density distributions in Fig. 17 that the vortex core becomes increasingly anisotropic with increasing f_y. We analyze this systematically by expanding the wave function of the ↓-component in an orthogonal basis set and quantifying the weights in the nth mode by a_n, as mentioned in Sec. IV C. In Fig. 18, we plot the weights a_n relative to a_0 computed for a half-quantum vortex state with $f_y = 1.0$. As we would expect, for the isotropic case with $f_y = 1.0$, $a_0 = 1$ and $a_n = 0$ for $n \neq 0$. As the trap anisotropy increases, we observe that the ground state is a mixture of $n \neq 0$ components as well. Nevertheless, we see that the trap anisotropy has a much smaller effect on the half-quantum vortex state than the anisotropy in the SO-coupling strength.

V. CONCLUSIONS

In summary, we have systematically investigated the ground condensate state of a spin-orbit coupled spin-1/2 Bose gas confined by a two-dimensional harmonic trap. The density distributions and collective density excitations have been obtained respectively by solving the Gross-Pitaevskii equation and the Bogoliubov equation, which are generalized to include spin-orbit coupling. We have found that

(1) The condensate is in a half-quantum vortex state if the intraspecies interaction g is smaller than interspecies interaction $g_{\uparrow\downarrow}$ and if the interaction strength is below a threshold g_c. We have calculated the threshold by monitoring the unstable quadrupole mode with an azimuthal angular momentum $m = -2$. A phase diagram for the half-quantum vortex state is therefore determined, as given in Figs. 1 and 14.

(2) The half-quantum vortex state (phase I) will turn into a superposition of two degenerate half-quantum vortex states (phase II A) if $g > g_{\uparrow\downarrow}$ and will start to involve high-order angular momentum components (phase II B) if $g > g_c$, where g_c depends on the ratio $g_{\uparrow\downarrow}/g$. The half-quantum vortex state is unstable against small anisotropies in the SO-coupling strength and large anisotropies in the trapping potential. The state tends to be a superposition of higher angular momentum states.

(3) In the presence of spin-orbit coupling, the behavior of collective density modes becomes complicated. In particular, the breathing mode with $\omega = 2\omega_\perp$ and the dipole mode with $\omega = \omega_\perp$ are no longer exact solutions of the many-body system.

(4) The condensate wave functions in the phases II A and II B are yet to be determined using the time-splitting spectral method for GPE. These wave functions break the rotational symmetry. We anticipate that interesting density patterns will emerge in the limit of very large interatomic interactions. Moreover, we anticipate that the phase II B in Fig. 1 will change to a density-stripe phase, while the phase II A will ultimately change to a plane-wave phase. The density-stripe and the plane-wave phases have been shown to be the mean-field ground state of a homogeneous spin-orbit-coupled Bose gas [8]. For the trapped system considered here, at large interaction strength, the effect of the trap becomes less important and our result therefore should be consistent with that of a homogeneous system. These are to be explored in future studies.

ACKNOWLEDGMENTS

We would like to thank Congjun Wu and Xiang-Fa Zhou for useful discussions. B. R. thanks Lin Dong and Hong Lu for useful discussions. H. H., X. J. L., and P. D. D. were supported by ARC Discovery Projects DP0984522, DP0984637 and DP0880404 respectively. H.P. was supported by the NSF, the Welch Foundation (Grant No. C-1669), and the DARPA OLE program.

[1] M. H. Anderson, J. R. Ensher, M. R. Matthews, C. E. Wieman, and E. A. Cornell, Science **269**, 198 (1995).
[2] K. M. O'Hara, S. L. Hemmer, M. E. Gehm, S. R. Granade, and J. E. Thomas, Science **298**, 2179 (2002).
[3] H. Hu, X.-J. Liu, and P. D. Drummond, New J. Phys. **12**, 063038 (2010).
[4] M. Greiner, O. Mandel, T. Esslinger, T. W. Hänsch, and I. Bloch, Nature (London) **415**, 39 (2002).
[5] Y.-J. Lin, K. Jiménez-García, and I. B. Spielman, Nature (London) **471**, 83 (2011).
[6] T. D. Stanescu, B. Anderson, and V. Galitski, Phys. Rev. A **78**, 023616 (2008).
[7] M. Merkl, A. Jacob, F. E. Zimmer, P. Ohberg, and L. Santos, Phys. Rev. Lett. **104**, 073603 (2010).
[8] C. Wang, C. Gao, C.-M. Jian, and H. Zhai, Phys. Rev. Lett. **105**, 160403 (2010).
[9] S. Gopalakrishnan, A. Lamacraft, and P. M. Goldbart, Phys. Rev. A **84**, 061604(R) (2011).
[10] T.-L. Ho and S. Zhang, Phys. Rev. Lett. **107**, 150403 (2011).
[11] Y. Zhang, L. Mao, and C. Zhang, Phys. Rev. Lett. **108**, 035302 (2012).
[12] Z. F. Xu, R. Lu, and L. You, Phys. Rev. A **83**, 053602 (2011).
[13] T. Kawakami, T. Mizushima, and K. Machida, Phys. Rev. A **84**, 011607(R) (2011).
[14] C. Wu, I. Mondragon-Shem, and X.-F. Zhou, Chin. Phys. Lett. **28**, 097102 (2011).
[15] X.-Q. Xu and J. H. Han, Phys. Rev. Lett. **107**, 200401 (2011).
[16] X.-F. Zhou, J. Zhou, and C. Wu, Phys. Rev. A **84**, 063624 (2011).
[17] J. Radić, T. Sedrakyan, I. B. Spielman, and V. Galitski, Phys. Rev. A **84**, 063604 (2011).
[18] H. Hu, B. Ramachandhran, H. Pu, and X.-J. Liu, Phys. Rev. Lett. **108**, 010402 (2012).
[19] S. Sinha, R. Nath, and L. Santos, Phys. Rev. Lett. **107**, 270401 (2011).
[20] H. Hu and X.-J. Liu, Phys. Rev. A **85**, 013619 (2012).
[21] T. Yefsah, R. Desbuquois, L. Chomaz, K. J. Gunter, and J. Dalibard, Phys. Rev. Lett. **107**, 130401 (2011).
[22] D. S. Petrov, M. Holzmann, and G. V. Shlyapnikov, Phys. Rev. Lett. **84**, 2551 (2000).
[23] A. Griffin, Phys. Rev. B **53**, 9341 (1996); P. A. Ruprecht, M. Edwards, K. Burnett, and C. W. Clark, Phys. Rev. A **54**, 4178 (1996); H. Pu and N. P. Bigelow, Phys. Rev. Lett. **80**, 1134 (1998).
[24] X.-J. Liu, H. Hu, A. Minguzzi, and M. P. Tosi, Phys. Rev. A **69**, 043605 (2004).
[25] X.-J. Liu, H. Hu, and P. D. Drummond, Phys. Rev. A **75**, 023614 (2007); **76**, 043605 (2007); **78**, 023601 (2008).
[26] M. M. Salomaa and G. E. Volovik, Phys. Rev. Lett. **55**, 1184 (1985).
[27] H. Pu and N. P. Bigelow, Phys. Rev. Lett. **80**, 1130 (1998).
[28] W. Bao, D. Jaksch, and P. A. Markowich, J. Comput. Phys. **187**, 318 (2003); W. Bao, Multiscale Model. Simul. **2**, 210 (2004).
[29] H. Wang, J. Comput. Appl. Math. **205**, 88 (2007).
[30] B. Binz and A. Vishwanath, Physica B **403**, 1336 (2008).
[31] S. Mühlbauer, B. Binz, F. Jonietz, C. Pfleiderer, A. Rosch, A. Neubauer, R. Georgii, and P. Böni, Science **323**, 915 (2009).
[32] D. A. W. Hutchinson, E. Zaremba, and A. Griffin, Phys. Rev. Lett. **78**, 1842 (1997).
[33] Jonas Larson and Erik Sjöqvist, Phys. Rev. A **79**, 043627 (2009). Here, the authors analyze how the non-Abelian gauge structure of spin-orbit-coupled BECs affects the dynamics.
[34] P. Ohberg and S. Stenholm, Phys. Rev. A **59**, 3890 (1999).
[35] S. Yi and H. Pu, Phys. Rev. A **73**, 061602(R) (2006).